Featured in Physics

Entangled Dual-Comb Spectroscopy

Abdulkarim Hariri,[1] Shuai Liu,[1] Haowei Shi,[2] Quntao Zhuang,[2,3] Xudong Fan,[4] and Zheshen Zhang[1,*]

[1]Department of Electrical Engineering and Computer Science, University of Michigan, Ann Arbor, Michigan 48109, USA
[2]Ming Hsieh Department of Electrical and Computer Engineering, University of Southern California, Los Angeles, California 90089, USA
[3]Department of Physics and Astronomy, University of Southern California, Los Angeles, California 90089, USA
[4]Department of Biomedical Engineering, University of Michigan, Ann Arbor, Michigan 48109, USA

(Received 13 March 2025; revised 28 June 2025; accepted 28 August 2025; published 15 October 2025)

Optical frequency combs have emerged as a cornerstone for a wide range of areas, including spectroscopy, ranging, optical clocks, time and frequency transfer, waveform synthesis, and communications. However, quantum-mechanical fluctuations of the optical carrier impose fundamental performance limits on the precision of classical optical frequency combs, particularly in their use for interferometry and spectroscopy. Entanglement, as a quintessential quantum resource, allows for surpassing the fundamental limits of classical systems. Here, we introduce entanglement into the realm of optical frequency combs, formulating entangled dual-comb spectroscopy (EDCS) that surmounts the fundamental limits of classical DCS. EDCS capitalizes on tailored entangled structures across the frequency comb, enabling simultaneous detection of all comb lines below the standard quantum limit of classical DCS. Applying EDCS in gas detection, we achieve a 2.6-dB enhancement in signal-to-noise ratio and a 1.7-fold reduction in integration time over classical DCS, rendering EDCS particularly suited for dynamic chemical and biological sensing, where fast, precise measurements subject to power constraints are required. EDCS opens a new avenue for exploiting quantum frequency combs, underscoring their prospects in a plethora of applications in precision metrology, spectroscopy, and timekeeping.

DOI: 10.1103/plh2-cr8s

Subject Areas: Quantum Information

I. INTRODUCTION

Entanglement is a quantum-mechanical property with no classical equivalent, exhibiting stronger-than-classical correlations shared by two or more objects. Since its initial discovery [1–3], entanglement has evolved from a subject for scientific debate to a transformative resource that enables capabilities beyond the limits of classical physics [4]. Entanglement, now a cornerstone of a broad range of quantum protocols for, e.g., quantum computing [5], quantum communication [6,7], quantum sensing [8–11], and quantum imaging [12], offers a pathway to surpass the fundamental limits arising from quantum-mechanical fluctuations [4]. In this regard, a key figure of merit for a quantum protocol is its advantage in, e.g., signal-to-noise ratio (SNR), measurement sensitivity, or integration time over what the best classical strategy affords subject to the same resource constraints for both regimes.

Optical frequency combs—a transformative tool comprising a spectrum of evenly spaced, phase-coherent laser lines—deliver exceptional performance in applications such as spectroscopy [13,14], ranging [15], optical clocks [16], and waveform synthesis [17]. In this context, dual-comb spectroscopy (DCS) has emerged as a powerful technique, renowned for its unmatched sensitivity and broad bandwidth achievable within a short measurement time. Nevertheless, DCS exemplifies a classical approach constrained by a fundamental trade-off between sensitivity and measurement time imposed by quantum noise. With recent DCS demonstrations exhibiting quantum-noise-limited performance [18–20], a pivotal question arises: How can quantum resources be leveraged within a DCS configuration, as achieved in gravitational-wave detection [21], distributed quantum sensing [22,23], and quantum illumination [24], to exceed such a fundamental limit?

Recently, protocols for quantum-enhanced spectroscopy [25,26] have emerged to overcome the fundamental limits of spectroscopy based on classical frequency combs. Specifically, Ref. [25] proposed a scheme that leverages

*Contact author: zszh@umich.edu

broadband squeezed light, electro-optic (EO) modulation, and homodyne detection to create a quantum frequency comb that would overcome the shot-noise limit of classical spectroscopy. However, without a dual-comb configuration, the practical bandwidth of optical measurements precludes the proposed scheme from achieving a wide spectral coverage on par with that of the DCS. In parallel, Ref. [26] devised a DCS protocol based on a quantum comb comprising squeezed individual lines detected by a local oscillator (LO) comb in a heterodyne configuration. Unfortunately, the generation of the desired quantum comb would be a formidable task, as it requires a nonlinear optical process with a phase-matching bandwidth narrower than the line spacing and a group-velocity-matching bandwidth as broad as that of the combs [26]. As such, while these schemes yield theoretically promising results, the experimental realization of a metrological advantage in quantum frequency-comb spectroscopy remains an outstanding challenge.

On the experimental front, squeezed dual-comb spectroscopy was recently reported [27], achieving a 3-dB SNR advantage over the compared *suboptimal* classical DCS protocol. While this work marks a meaningful step toward incorporating nonclassical resources into dual-comb architectures, it has not established a metrological quantum advantage due to the lack of a comparison against the *optimal* classical configuration subject to the same power constraint for both the quantum and classical regimes [28]. In Sec. II A and Appendix B, we provide a formal theoretical analysis to identify the optimal performance limits of dual-comb spectroscopy with both classical and quantum resources. Such benchmarking is essential for substantiating claims of quantum advantages in metrological protocols.

Here, we introduce and experimentally demonstrate entangled dual-comb spectroscopy (EDCS) that overcomes the fundamental limits of classical DCS. Unlike squeezed DCS [27] based on amplitude soliton squeezing produced from a Kerr-nonlinear fiber system, EDCS exploits a bright quantum comb with nonclassical correlations across matched comb lines, generated by displacing a family of two-mode squeezed states from spontaneous parametric down-conversion (SPDC) with a classical comb. While single-mode squeezing allows for measuring only one quadrature below the shot-noise level, entanglement embedded in two-mode squeezed states opens the door to sub-shot-noise detection of *both* the amplitude and phase quadratures, as demonstrated in quantum-dense metrology [29]. By harnessing the entangled spectral structure across a large number of optical modes produced concurrently in an SPDC process, EDCS enables simultaneous detection of all comb lines below the standard quantum limit (SQL), with a demonstrated SNR enhancement of 2.6 dB compared to classical DCS and a reduction in integration time by a factor of 1.7. Our experiment establishes a robust framework for integrating quantum resources into DCS, paving the way for transformative advancements in high-precision sensing and metrology.

II. PRINCIPLE OF EDCS

Our approach to EDCS requires the use of three frequency-comb sources: an entangled comb to provide the quantum correlations needed to achieve sub-SQL performance; a classical comb that coherently displaces the entangled comb to produce a bright entangled signal comb transmitted to the sample; and a classical LO comb to simultaneously measure all entangled signal comb lines. The experimental schematic of EDCS shown in Fig. 1 illustrates the interplay between the three comb sources. The experiment begins with a cw 1550-nm fiber laser, which seeds an optical parametric oscillator (OPO) cavity to generate an entangled comb [30] described by the following Hamiltonian in the interaction picture [31]:

$$\hat{H} = i\hbar\chi \sum_{n=0}^{N} (\hat{a}^{\dagger}_{S_{-n}} \hat{a}^{\dagger}_{S_n} - \hat{a}_{S_{-n}} \hat{a}_{S_n}), \tag{1}$$

where $\hat{a}_{S_n}$ and $\hat{a}^{\dagger}_{S_n}$ are the annihilation and creation operators, respectively, of the nth mode of the entangled comb, $\hbar$ is the reduced Planck constant, and χ quantifies the strengths of the nonlinear interaction. Here, $\hat{a}^{\dagger}_{S_{-n}} \hat{a}^{\dagger}_{S_n}$ ($\hat{a}_{S_{-n}} \hat{a}_{S_n}$) describes the creation (annihilation) of a pair of photons in the nth and $-n$th modes through SPDC. All mode pairs undergo parallel SPDC processes to produce an entangled comb with a spectral structure comprising a central comb line in a displaced single-mode squeezed state, while the remaining comb lines form pairs of two-mode squeezed vacuum (TMSV) states as depicted in Fig. 2. The spacing between the comb lines must be a multiple of the free spectral range of the OPO cavity and is set to 17.565 GHz in the experiment to accommodate the resolution of the programmable optical filter used to engineer the classical and LO combs. The total number of entangled comb lines, N, is determined by the phase-matching bandwidth of the SPDC over the free spectral range of the OPO cavity. At the quantum source, only the central comb line carries tens of microwatts of optical power, while the remaining lines are in TMSV states. To produce a bright entangled signal comb employed to interrogate the sample, the entangled comb interferes with a spectrally matched classical comb on an unbalanced beam splitter, converting each TMSV pair into a displaced two-mode squeezed state, with an optical power level up to several hundred microwatts per comb line. After probing the sample, the entangled signal comb is measured in a heterodyne configuration, where it beats with an LO comb. Both the LO and signal combs are generated from a common continuous-wave (cw) laser, each undergoing EO modulation and spectral shaping via separate

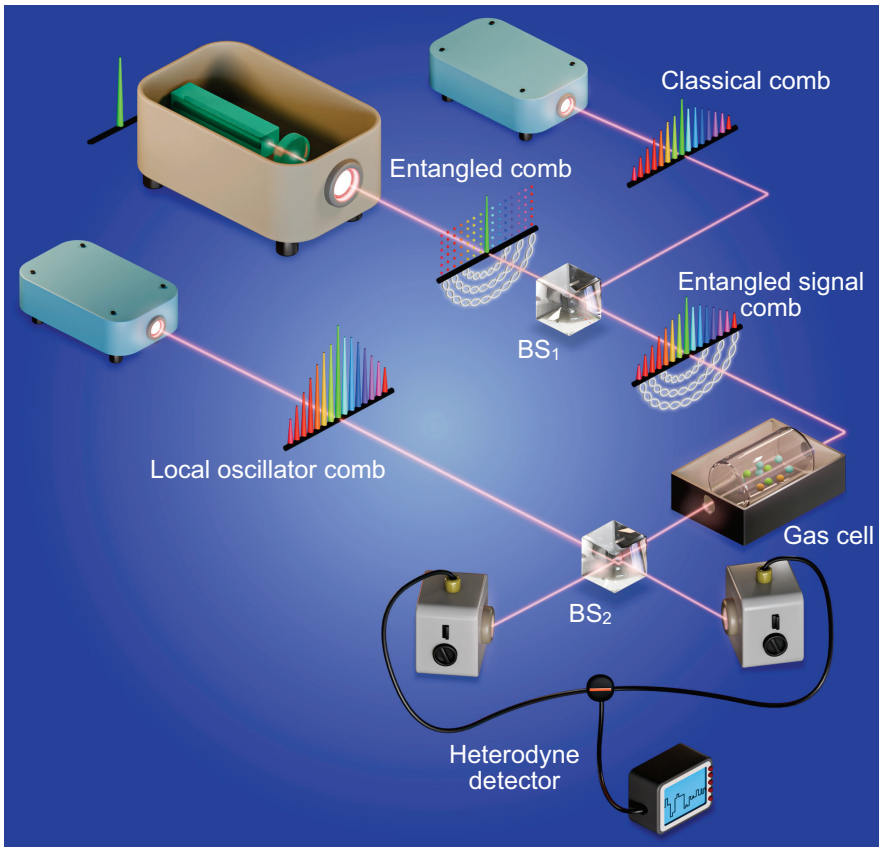

FIG. 1. Experimental setup for entangled dual-comb spectroscopy. An entangled optical frequency comb is coherently displaced by a classical comb at BS_1 to generate a bright entangled signal comb. This signal comb is transmitted through a gas sample for spectroscopic analysis. The absorption fingerprint of the gas is retrieved through an interferometric measurement with a local oscillator comb in a heterodyne detection configuration. The protocol exploits the sub-SQL capabilities of the entangled comb to achieve a higher sensitivity and a reduced integration time compared to classical dual-comb spectroscopy. Double helix: entanglement shared by the comb lines. Dotted lines: two-mode squeezed vacuum states.

modulators and programmable optical filters that configure the intensity and phase of each comb line. In the experiment, the EO modulation frequency on the LO comb defines the repetition rate f_{rep} of the DCS system and is chosen to 17.565 GHz, matching the lines of the entangled comb. The classical comb is modulated at a frequency offset from f_{rep} by $\delta f_{\mathrm{rep}} = 4$ MHz. By doing so, a radio-frequency (rf) comb with a δf_{rep} line spacing is generated via the beating between the LO and entangled signal comb in the heterodyne detection and is subsequently acquired and processed by electronics. The accessible bandwidth of the entangled signal comb is 0.17569 THz, limited by the power roll-off of the LO and classical combs at large mode indices (see more experimental details in Sec. IV and Appendix A). The EDCS protocol is benchmarked against the SQL defined by a classical quantum-noise-limited DCS protocol based on the same classical- and LO-comb configuration while the entangled comb is turned off.

The entanglement structure embedded in the entangled signal comb and its spectral configuration along with that of the LO comb are illustrated in Fig. 2. The OPO cavity generates a single-mode squeezed state at the center and an entangled comb comprising pairs of TMSV states, as represented by the connected dotted lines and quantum operators $\hat{a}_{S_n}$ and $\hat{a}_{S_{-n}}$, that are multiples of f_{rep} away from the central cavity resonance, where f_{rep} is determined by the free spectral range of the OPO cavity. The linewidth $\Delta\nu$ of the OPO cavity is sketched with the Lorentzian shape. The classical comb's line spacing differs from that of the entangled comb by δf_{rep} such that the interference between the two combs on BS_1 (as shown in Fig. 1) leads to displacements α_{S_n} at frequencies $n(f_{\mathrm{rep}} + \delta f_{\mathrm{rep}})$, as represented by the red lines. The LO comb's line spacing is aligned with that of the entangled comb at f_{rep}, allowing all entangled signal comb lines to be simultaneously measured at a quantum fluctuation level below that of the SQL by virtue of the property of the entanglement embedded in the TMSV states. At the same time, the beating between the LO comb line at nf_{rep} and the displacement on the entangled signal comb at $n(f_{\mathrm{rep}} + \delta f_{\mathrm{rep}})$ translates to a beat

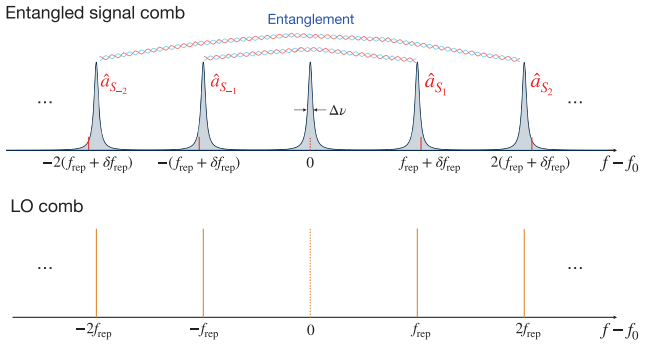

FIG. 2. Entanglement structure and spectral configuration of entangled signal and LO combs. $\hat{a}_{S_n}$ and $\hat{a}_{S_{-n}}$ form pairs of TMSV states produced from the OPO cavity, constituting an entangled comb. The line spacing of the LO comb is locked to that of the entangled comb at f_{rep}, allowing for simultaneous detection of all entangled signal comb lines below the SQL. The classical comb displaces the entangled comb by α_{S_n} at frequencies $n(f_{\mathrm{rep}}+\delta f_{\mathrm{rep}})$ to produce a bright entangled signal comb. The central dashed comb lines are employed solely for phase locking. f_0 is the central frequency of the frequency combs.

note at $n\delta f_{\mathrm{rep}}$ in the rf spectrum. The aliasing arising from the beating of the $\pm n$th lines of the entangled signal and LO combs is resolved by appropriately designing the displacement at each line (see Sec. IV). The rf spectrum resulting from the beating of the entangled signal or classical signal comb with the LO comb is depicted in Fig. 3(a), demonstrating enhanced SNR of 2.6 dB endowed by the entangled comb structure. To account for the increased phase noise at

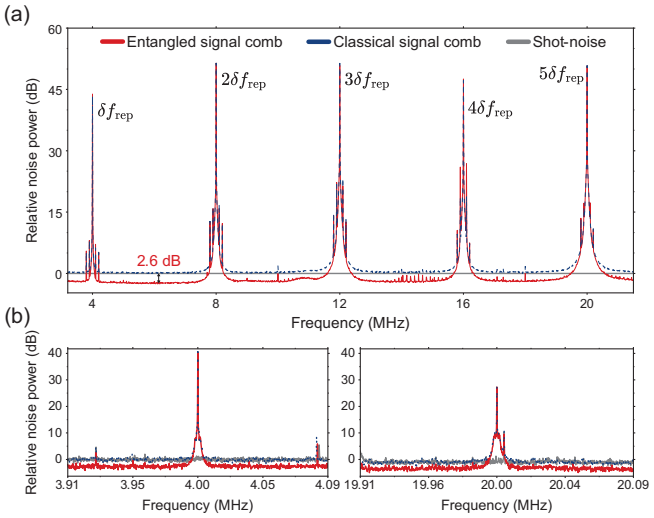

FIG. 3. rf spectra of entangled dual-comb and classical dual-comb. (a) rf spectrum obtained from the beating of the entangled signal comb or classical signal comb with the local oscillator comb. Enlarged rf spectra at the first [(b), left] and fifth [(b), right] beat notes obtained under reduced power levels of the classical signal comb. Operating at lower power mitigates the phase noise on the recorded beat notes.

higher beat notes, the power of the classical signal comb is deliberately reduced. This adjustment ensures an expanded bandwidth for shot-noise-limited measurements, as illustrated in Figs. 3(b) and 3(c).

A. Classical and quantum DCS benchmarks

Appendix B entails a general benchmarking for the classical DCS and EDCS. Here, we present SNR benchmarks for a uniform comb and squeezing spectrum in the weak absorption regime to intuitively illustrate the advantage of EDCS over classical DCS, while the subsequent sections adopt the general theory that does not resort to such premises in analyzing the experimental data and benchmark against classical DCS protocols. In the scenario of uniform combs, the comb line amplitudes $\{A_n\}$ and $\{B_n\}$ for the entangled signal and LO combs and squeezing gains $\{G_n\}$ defined in Appendix B are set to uniform, i.e., $A_n = A, B_n = B$, and $G_n = G$, and the power transmissivities $\{\kappa_n\}$ of the absorption spectrum approach unity, i.e., $\kappa_n \to 1$, where n is the comb line index. In addition, the LO comb is assumed much brighter than the signal comb, i.e., $|B| \gg |A|$, and does not interact with the sample.

As a standard practice of quantum metrology, we first define the power constraint as a pivotal parameter for equitable comparisons between different protocols. In an *asymmetric* EDCS system in which only one comb interfaces with the sample, such a constraint is imposed by the total amount of power $P = \hbar\omega_c A^2 M/T$ that the sample is exposed to, where M is the total number of comb lines. The SNR of heterodyne detection can be derived from Eq. (B17) as

$$(\mathrm{SNR}_m|_{\kappa_n\to 1})^2 = \frac{A^2B^2}{M(B^2/2G + A^2/2)} \approx \frac{A^2}{M/2G} \qquad (2)$$

in the limit of $B^2 \gg A^2$, viz., the strong LO limit. Physically, the denominator is interpreted as the total noise variance contributed by $M/2$ two-mode-squeezed mode pairs beating with their associated LO modes. The amplitude of each LO mode is B, so the shot-noise variance of a pair of LO modes in heterodyne detection is B^2, while two-mode squeezing reduces the variance to B^2/G. As such, the noise variance accounting for all $M/2$ mode pairs amounts to $MB^2/2G$.

Setting $G = 1$, the classical limit (CL) of SNR is found to be

$$(\mathrm{SNR}_{\mathrm{CL}}^{\mathrm{asym}})^2 = \frac{A^2}{M/2} = \frac{2PT}{M^2\hbar\omega_c}. \qquad (3)$$

Following a similar formalism, the SNR for *symmetric* EDCS [14] in which two combs combine on a 50:50 beam splitter and subsequently pass through the sample is established as

$$(\mathrm{SNR}_{\mathrm{C}}^{\mathrm{sym}})^2 = \frac{A^2B^2}{M(A^2+B^2)/2}, \tag{4}$$

as shown in Eq. (B20). Akin to asymmetric DCS, setting P, the total optical power impinging on the sample, as the constraint, the classical limit for SNR of symmetric DCS is obtained by equalizing the power carried on the two combs, i.e., $A^2 = B^2 = PT/M\hbar\omega_c$, yielding

$$(\mathrm{SNR}_{\mathrm{CL}}^{\mathrm{sym}})^2 = \frac{PT}{M^2\hbar\omega_c}, \tag{5}$$

in agreement with DCS's shot-noise-limited SNR presented in Ref. [14]. In Ref. [27]'s squeezed DCS experiment, one comb is about 3 orders of magnitude more intense than the other, rendering its SNR more than 2 orders of magnitude inferior to the classical limit as given by Eq. (5), achieved by two equal power combs. In such an unbalanced scenario of Ref. [27]'s experiment, the measurement noise is dominated by the shot noise from the intense comb, and, thus, squeezing that comb achieves an SNR advantage over a classical DCS scheme employing the same unbalanced power on the two combs. One may wonder if the quantum advantage would persist should the power carried on the squeezed comb and the classical comb be balanced. Unfortunately, by doing so the classical comb would pick up the noise in the antisqueezed quadrature of the squeezed comb in their beating as the authors of Ref. [27] recently verified [32], which precludes an SNR advantage over the optimal classical DCS subject to the power constraint. As such, achieving a quantum advantage in DCS requires meticulous design and implementation of the quantum states of both combs, as we accomplish in the current experiment.

III. ENTANGLEMENT-ENHANCED GAS DETECTION

We next demonstrate EDCS for gas detection in an asymmetric scheme, in which only the entangled signal comb is directed to the sample of interest, minimizing the risk of sample damage while maintaining a high SNR and effective technical noise suppression achieved through the use of a strong LO comb and balanced detection. Figure 4 (a) shows the optical spectrum of the LO comb with a line spacing of $f_{\mathrm{rep}} = 17.565$ GHz, selected to align with the free spectral range of the OPO cavity that generates the entangled frequency comb while amenable to the resolution of the programmable optical filter. To achieve a finer spectral resolution, we reposition the cw seed laser to 50 distinct central frequencies and acquire a dual-comb spectrum at each setting. These spectra, each comprising comb lines with a 17.565 GHz spacing, are interleaved offline to synthesize a broadband spectrum with an effective resolution of approximately 350 MHz, set by the designed sweep step size across 50 acquisitions, as depicted

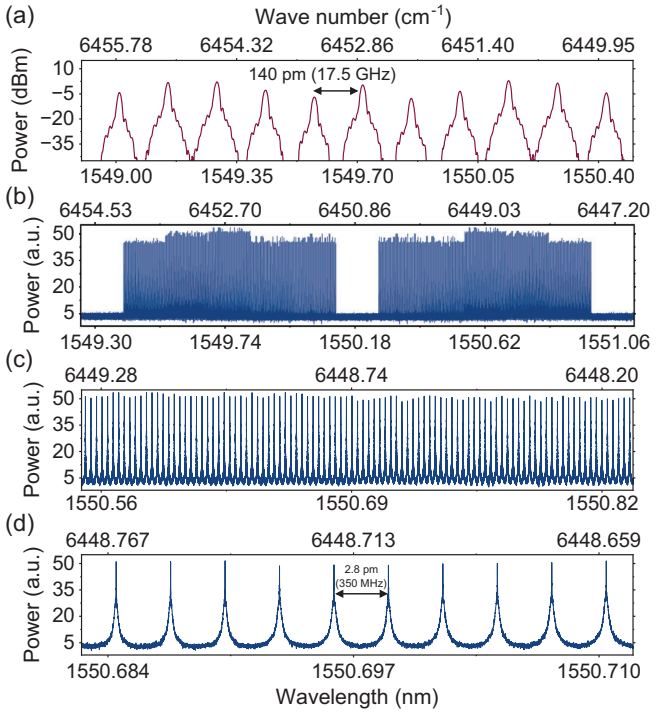

FIG. 4. Measured local oscillator and dual-comb spectra. (a) Spectrum of the local oscillator comb measured using an optical spectrum analyzer. (b) Dual-comb spectrum obtained by sampling the time-domain signal of the subtracted photocurrents from the balanced receiver at a 100 MHz sampling rate for 0.5 s. The data are postprocessed to derive the frequency-domain spectrum. The larger number of comb lines is achieved by sweeping the center frequency of the cw laser. (c) An enlarged view of a 35 GHz bandwidth, highlighting the mode-resolved nature of the dual-comb spectrum. (d) A further enlargement to a 3.5 GHz bandwidth, resolving individual comb lines.

in Figs. 4(b)–4(d). The central region of the spectrum displays no comb lines due to a zero carrier-offset frequency, resulting in the absence of observable beat notes. In the experiment, the central lines of the three combs are utilized to phase lock the entangled comb displacement and to lock the LO comb to the squeezed quadratures. Both locking units are essential for maintaining stability in the EDCS measurements.

In gas detection, the entangled signal comb with $\delta f_{\mathrm{rep}} = 4$ MHz passes through a gas cell containing hydrogen cyanide (HCN) at a pressure of 25 Torr, with an optical path length of 17.5 cm, yielding an absorption depth of 3 dB. To obtain the absorption spectrum of HCN, we use the comb configuration and cw laser sweep, the same as that in Fig. 4(b). Figure 5(a) shows the measured average transmittance spectrum, which is fitted to a model based on the HITRAN2020 database [33] built on the optical path length, pressure, temperature, and concentration as input parameters, showing excellent agreement between the experimental data and model. To demonstrate the speedup enabled by EDCS, we estimate the precision of the

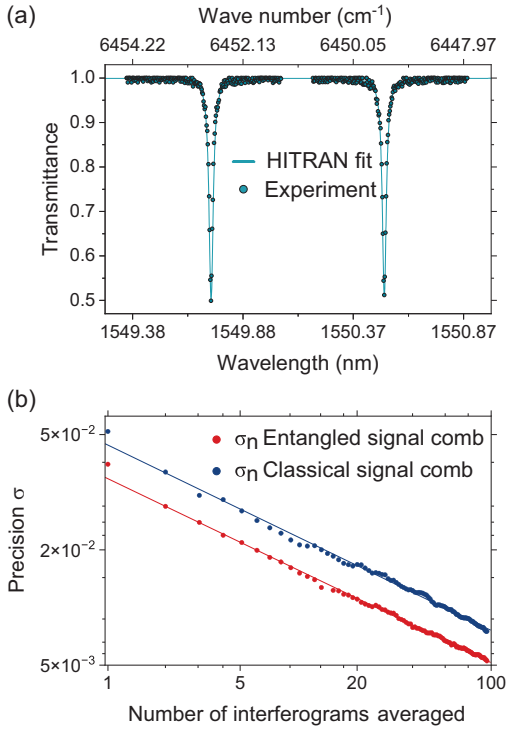

FIG. 5. Measured absorption spectrum and quantum speedup. (a) Acquired absorption spectrum through EDCS and fit with HITRAN database, showcasing its accuracy. The standard deviation of the differences (HITRAN fit—experiment) is 1.1%, with a maximum difference of less than 7% observed near peak absorption values. (b) Quantum speedup of EDCS over classical DCS enabled by enhanced precision below the standard quantum limit.

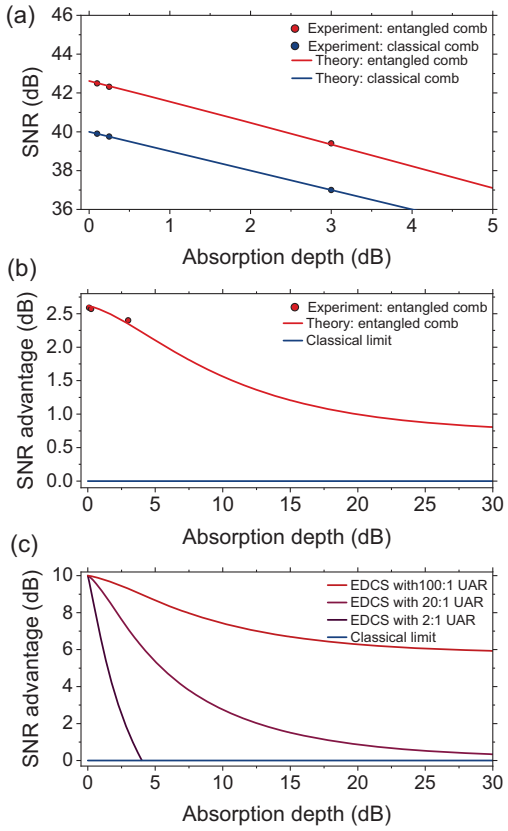

FIG. 6. Robustness of EDCS's quantum advantage against sample absorption. (a) SNR of EDCS and classical DCS as a function of increasing absorption depth in gas cells. Despite the heightened attenuation at moderate depths, the quantum advantage of EDCS over classical DCS remains evident. The standard deviation of each experimental data point is 0.6 dB. (b) SNR advantage of EDCS over classical DCS, illustrating the moderate degradation rate of the quantum advantage with increasing absorption and its eventual saturation. The standard deviation of each experimental data point is 0.08 dB. (c) Simulation of a flattop entangled comb with 10 dB maximum squeezing and 15 dB maximum antisqueezing, measured using a flattop LO, demonstrating the required unattenuated-to-attenuated ratio (UAR) of comb lines to sustain a target quantum advantage level.

transmittance spectrum measurement as a function of the number of averaged interferograms. The interferograms are detected using a balanced photodetector and recorded on an oscilloscope with sufficient bandwidth and a sampling rate of 100 MS/s. After filtering, a 10 μs segment of the time-domain signal is extracted, corresponding to a single interferogram with a resolution bandwidth of 100 kHz. Figure 5(b) illustrates the precision as a function of the number of averaged interferograms, highlighting that EDCS achieves a quantum speedup factor of 1.7 compared to classical DCS in reaching a target precision. This advancement underscores the prospect of EDCS to overcome the fundamental trade-off between sensitivity and measurement time, paving the way for sensing applications with boosted speed and precision.

We further evaluate EDCS's performance under varying absorption depths, as illustrated in Fig. 6. The single-line SNR (SNR_m, formally defined as the power SNR for estimating the spectrum κ_m at the mth line; see Appendix B) for both EDCS and DCS is shown in Fig. 6(a). Additionally, the SNR advantage in the simultaneous detection of all comb lines at different absorption depths is shown in Fig. 6(b). Notably, the quantum advantage remains largely intact even with 3 dB absorption, compared to lower absorption levels of 0.1 and 0.25 dB. This robustness results from a synergistic interplay between the classical and quantum resources in our configuration. EDCS leverages the sub-SQL performance provided by the nonclassical properties of TMSV states, while its distributed nature minimizes the impact of losses on quantum advantage, as only a small fraction of the comb lines is expected to experience loss in a spectroscopic measurement. Crucially, a favorable unattenuated-to-attenuated ratio (UAR) of comb lines—10:1 in our setup—results in minimal degradation of sub-SQL performance. To further illustrate EDCS's capability, we simulate the performance of a flattop entangled comb with a maximum of 10 dB squeezing and 15 dB antisqueezing, measured using

a flattop LO. The results, shown in Fig. 6(c), highlight the resilience of entangled combs to loss, attributed to their high UAR of comb lines.

IV. DISCUSSION

We implement linear-absorption DCS fueled by entangled spectral structures to achieve an enhanced SNR, higher measurement sensitivities, and reduced integration times. Our experimental setup introduces an additional servo loop to lock the relative phase between the entangled comb and the classical signal comb, while all other feedback loops mirror those used in conventional TMSV sources. To meet the tighter phase requirements and overcome the locking challenges in EDCS, our experiment hinges on two key techniques. (i) EO comb generation: A single cw laser seeds the optical cavity and, via EO modulation, simultaneously feeds the classical signal and LO combs. This common seed guarantees intrinsic mutual coherence [34], enabling sub-shot-noise detection of the entangled signal comb, shot-noise-limited detection of the classical comb, and robust phase locking to the LO. (ii) Programmable optical filtering: A wave shaper precisely sets the amplitude and phase of both the classical signal comb and the LO comb. Although the entangled comb never passes through the filter, its effective quadrature orientation and power distribution are indirectly tuned via coherent displacement by the classical comb. Such control is pivotal for the phase-sensitive heterodyne detection: The nonuniform spectral phase across the LO comb introduced by EO modulation must be corrected so that all squeezed quadratures align. Moreover, the spectral phase profile of the classical comb must align with that of the LO comb to maximize beat-note strength. Phase misalignment would diminish the quantum enhancement due to increased noise power caused by mixed squeezed and antisqueezed quadratures or reduced signal power as a result of misaligned phases between the signal and LO combs. The programmable filter also equalizes optical power across modes and suppresses excess phase noise in the rf spectrum by attenuating lines where necessary. To confirm that the observed 2.6-dB quantum advantage is genuine—and not an artifact of the filter settings—we record dual-comb spectra with identical wave shaper configurations while toggling the quantum comb on and off. The enhancement remains unchanged, verifying the robustness of our EDCS scheme.

With the current entanglement and spectral configurations, the beatings between the nth and $-n$th entangled signal and LO comb lines are translated into the same rf frequency at $n\delta f_{\mathrm{rep}}$. We have developed two approaches to resolve the aliasing (see Appendix B). The first approach entails two-shot measurements, in which the positive-index entangled comb lines are displaced by α_{S_n} and $-\alpha_{S_n}$ in the two consecutive measurements. Since the beat note at $n\delta f_{\mathrm{rep}}$ in the two measurements yields $\alpha_{S_{-n}} + \alpha_{S_n}$ and $\alpha_{S_{-n}} - \alpha_{S_n}$, the sum and the difference of the two measurements unveil $2\alpha_{S_{-n}}$ and $2\alpha_{S_n}$ without compromising the overall SNR. In the second approach, the positive- and negative-index comb lines are displaced along two different quadratures, mathematically described as real and imaginary displacements, respectively. The beatings of the nth and $-n$th entangled signal and LO comb lines then yield rf signals proportional to $\cos(2\pi n\delta f_{\mathrm{rep}}t)$ and $\sin(2\pi n\delta f_{\mathrm{rep}}t)$, allowing the positive- and negative-index comb lines to be unambiguously separated by two rf mixers.

It is worth noting that the demonstrated EDCS protocol differs from that proposed in Ref. [26] in both the structure of the quantum comb and the measurement scheme. Specifically, Ref. [26] employs a collection of single-mode squeezed states, where the comb lines exhibit no cross-line correlations. In contrast, the quantum comb used in this work features comb lines that are pairwise entangled (two-mode squeezed). The quantum correlations between quadratures, as opposed to polarizations, of the entangled modes endow EDCS's enhancement. This approach enables the use of standard TMSV sources while paving the way for integration into $\chi^{(3)}$ complementary metal-oxide-semiconductor-compatible silicon-photonics platforms. These platforms have made significant advancements in quantum-light generation [35–40], closing the gap with bulk quantum sources that hold the record of the amount of measured squeezing [41]. Moreover, these platforms offer the potential to tailor the dispersion profile [42,43] to generate ultrabroadband quantum combs and to integrate classical Kerr frequency combs in tandem with programmable optical filters [44] as the LO comb, opening a new avenue for the development of highly compact and versatile EDCS platforms capable of outperforming their classical counterpart [45].

As highlighted in Refs. [18,46,47], the limited spectral span—and, in our case, a smaller number of comb lines—characteristic of DCS using EO modulators is effectively mitigated through the frequency tunability of the cw laser and rf synthesizers. This agility allows for precise adjustments to the center frequency and repetition frequency of the combs, providing substantial flexibility in experimental configurations. Despite these constraints, this approach delivers a high SNR within short measurement times and enables customizable spectral resolution. With the current configuration, the spectral resolution of our EDCS setup is 350 MHz shown in Fig. 4(d). To address the remaining gaps within these intervals, the rf can be swept by ± 175 MHz at each laser center frequency. This two-step process guarantees complete spectral coverage while maintaining the quantum advantage, as all comb lines remain well within the 400 MHz squeezing bandwidth of the entangled comb source throughout both laser and rf sweeps. As for further expanding the spectral coverage, various techniques have been proposed and demonstrated. For instance, efficient nonlinear broadening can be used to

achieve wider bandwidths with high resolution, as demonstrated in Ref. [48]. Additionally, cascading EO modulators, as shown in Ref. [49], offers another effective method for significantly increasing spectral coverage.

EDCS's advantage over classical DCS can be further broadened via multiple routes. First, the maximum amount of vacuum squeezing produced by our entangled-comb source is measured at approximately 4 dB, while sources delivering over 10 dB of squeezing have been reported [41]. Second, the rf synthesizer employed in the present experiment exhibits a phase noise level at -75 dBc/Hz at 10 GHz frequency with a 10-kHz offset, while a standard commercially available unit offers -132 dBc/Hz at 10 GHz to further amplify the disparity in the integration times between EDCS and classical DCS. Third, mitigation of experimental imperfections, such as inaccuracies in the wave shaper phase filter configurations, subunity fringe visibility (97%) due to mode mismatch between the entangled signal and LO combs, and limited quantum efficiency of the photodiodes (88%), will reduce mixing of the squeezed and antisqueezed quadratures and the amount of vacuum noise mixed in, enabling an even more pronounced quantum advantage for EDCS.

We note that the theoretical results shown in Fig. 6(c) can be further optimized by analyzing Eq. (B17) (see Appendix B), illustrating the additional degrees of freedom and key considerations when transitioning from DCS to EDCS. One optimization approach involves minimizing antisqueezing by operating the OPO cavity at lower pump powers, without degrading the squeezing. This reduces the contribution of antisqueezing to the degradation of quantum advantage observed in Fig. 6(c). A second approach employs adaptive measurements to configure the LO in a manner that mimics the imbalance in intensity caused by absorption loss on the signal comb. This further mitigates the impact of antisqueezing on the system's performance. These dependencies highlight the intricate nature of EDCS and underscore its potential for significant metrological advantages.

Before closing, we compare our work with the two recently reported quantum DCS experiments [27,50]. A figure of merit for DCS is the quality factor defined as $\mathrm{SNR} \times M/\sqrt{\tau}$, where $M = 2N$ is the total number of comb lines, SNR is defined in amplitude, and τ is the integration time [14]. The asymmetric DCS scheme, in which only the signal comb interrogates the sample while the other much more intense comb serves as an LO at the heterodyne detector, is known to saturate classical DCS's quality-factor limit given the power on the sample [26]. Exploiting entanglement to enhance the SNR, thus, enables our asymmetric EDCS to surpass the fundamental limit of classical DCS. Reference [27]'s experiment is innovative, offering large spectral coverage and high resolution. However, in its symmetric DCS scheme, the optimal quality factor subject to the same power constraint is achieved by evenly distributing the optical power over the two combs. Consequently, the large imbalance between the power levels of the two combs in the experiment results in a quality factor that falls short of the classical limit (see Appendix B). Reference [50]'s experimental DCS scheme is asymmetric based on a classical comb interrogating the sample and a squeezed LO. While such a configuration may offer some practical benefits due to the low frequency conversion efficiency, it cannot beat the fundamental limit of classical DCS [51].

ACKNOWLEDGMENTS

This work is supported by Office of Naval Research Grant No. N00014-23-1-2296, National Science Foundation Grants No. 2317471 and No. 2326746, and University of Michigan. Q. Z. and H. S. also acknowledge support from U.S. Air Force Office of Scientific Research MURI FA9550-24-1-0349 and DARPA D24AC00153-02. A. H. acknowledges a scholarship from the National Company of Telecommunication and Information Security. We thank J. Wu for discussion on phase locking.

DATA AVAILABILITY

The data that support the findings of this article are not publicly available because of legal restrictions preventing unrestricted public distribution. The data are available from the authors upon reasonable request.

APPENDIX A: EXPERIMENTAL DETAILS

1. EDCS setup

A detailed experimental diagram is shown in Fig. 7. A 1550-nm fiber laser (NKT Photonics Koheras BASIK) generates 30 mW of light, which is modulated by a fiber-based EO phase modulator (PM) driven at 88 MHz to create sidebands for cavity locking via the Pound-Drever-Hall technique. The modulated light is amplified to approximately 1.5 W by an erbium-doped fiber amplifier (EDFA) and coupled into free space. The 1550-nm light is directed to a three-mirror cavity for spatiotemporal mode cleaning (MC) and locked at its maximum transmission. The output from the MC cavity is then split into two arms: One serves as the pump for second-harmonic generation (SHG), while the other passes through a second MC cavity and is subsequently split into three arms to serve as the seed for the OPO, the classical comb, and the LO comb for heterodyne measurements.

The classical comb is generated using two fiber-based EO-PMs: one driven at 17.569 GHz to create the comb lines and another driven at 100 kHz by a lock-in amplifier to generate sidebands for locking the classical comb to the entangled comb. Prior to interfering with the entangled comb, the classical comb passes through a programmable optical filter (wave shaper) to control the intensity and

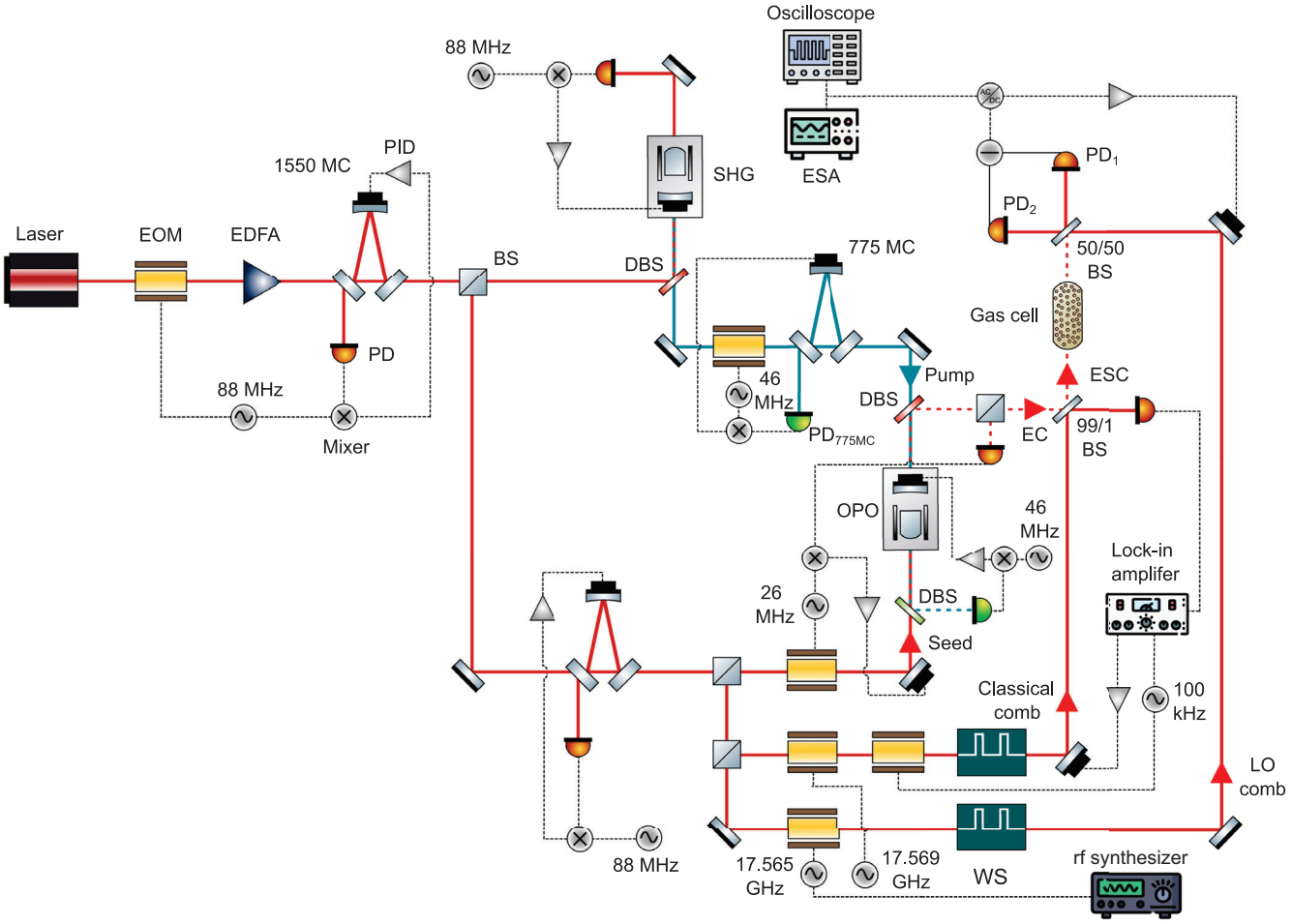

FIG. 7. Schematic of the experimental setup. An entangled comb at a wavelength of 1550 nm is generated in a doubly resonant OPO operated below threshold. EOM: electro-optical modulator; EDFA: erbium-doped fiber amplifier; 1550MC: three-mirror cavity for spatiotemporal mode cleaning of 1550 nm light; PID: proportional-integral-derivative controller; BS: beam splitter; DBS: dichroic beam splitter; SHG: second harmonic generation; PD: photodiode. To generate the entangled signal comb, the entangled comb is interfered with a classical comb, generated via an EOM followed by a wave shaper (WS), on a 99/1 BS. To lock the phase between the classical comb and entangled comb, a lock-in amplifier drives a second EOM on the classical comb arm to generate sidebands for the error signal, which is used by a PID controller to stabilize the phase. The entangled signal comb passes through a gas cell, after which it interferes with the LO comb in a heterodyne configuration. The subtracted photocurrent from balanced detection is analyzed by an electronic spectrum analyzer (ESA) for real-time optimizations of the system, while an oscilloscope is used for interferogram acquisition.

phase of each line of the entangled signal comb. The wave shaper balances the intensities of the two comb lines forming each pair, deliberately reduces the power of all comb lines (except the central comb line used for locking) to mitigate phase noise in the rf beat notes [Figs. 3(b) and 3(c)], and optimizes the phase of each comb line to maximize rf beat notes. Additionally, it configures the comb phase for the two-shot measurements used to resolve comb aliasing.

The SHG cavity is a semimonolithic design incorporating a curved mirror with low reflectivity at 775 nm and high reflectivity at 1550 nm, along with a periodically poled $KTiOPO_4$ (PPKTP) crystal. It is locked using the 88-MHz sidebands and generates 775-nm light through second-order frequency doubling. The 775-nm light is directed to an MC cavity before being injected into the OPO cavity, which contains an identical PPKTP crystal. The OPO cavity's curved mirror has high reflectivity at 775 nm and moderate reflectivity at 1550 nm. The three MC cavities are locked by tapping the reflected light from their input coupling mirrors, while the SHG cavity and the OPO's 1550- and 775-nm locks are achieved by tapping their transmitted beams.

To generate an entangled comb, the weak 1550-nm seed beam is modulated using a free-space PM driven at 40 MHz, creating sidebands for parametric amplification locking. The OPO cavity is locked using a 66-MHz sideband of the 775-nm pump, which transmits through the DBS on the pump input path. When pumped with 775-nm light, the OPO generates squeezed light via

SPDC at 1550 nm, and, when phase locked to achieve parametric amplification, altering the seed's photon statistics from a coherent state to a displaced phase-squeezed state. The quantum light emitted from the OPO comprises a single-mode squeezed state at the central frequency and an entangled comb consisting of pairs of TMSV states. After its generation, the entangled comb is interfered with a classical comb on a 99/1 beam splitter, converting each TMSV pair into a displaced two-mode squeezed state.

2. Characterization of entangled comb

The LO comb is prepared in a manner similar to the classical comb, using a separate PM and a wave shaper. The LO comb's amplitudes and phases are adjusted to align with the squeezed quadratures of the TMSV states, enabling simultaneous measurement of maximum squeezing across all entangled comb lines. Without proper amplitude balancing, the LO is not matched to the signal comb, resulting in reduced observed squeezing. Furthermore, improper phase alignment results in mixing of squeezed and antisqueezed quadratures from different modes, nullifying the overall sub-SQL capabilities of the entangled comb. Figures 8(a)–8(f) illustrate the measured squeezed and antisqueezed quadratures for the central comb line and five two-mode pairs. Figure 8(g) demonstrates simultaneous detection of the squeezed quadratures for all two-mode squeezed states, while Fig. 8(h) demonstrates the

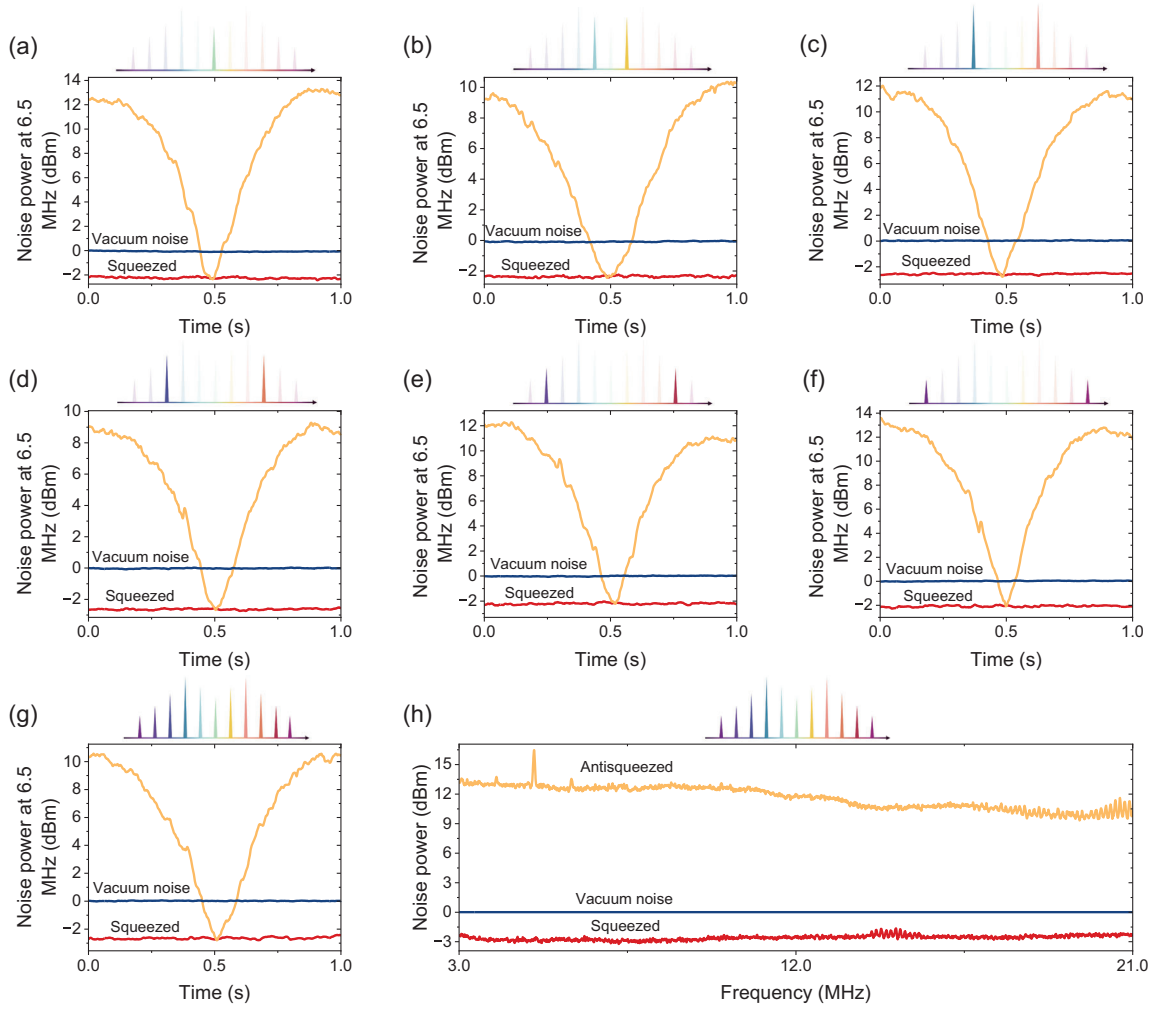

FIG. 8. Zero-span measurements of the entangled comb at a frequency of 6.5 MHz, captured using an electrical spectrum analyzer. (a) Measurement of the central comb line using LO's central comb line, while all other comb lines are off. (b) Measurement of the first entangled mode pair. (c) Measurement of the second entangled mode pair. (d) Measurement of the third entangled mode pair. (e) Measurement of the fourth entangled mode pair. (f) Measurement of the fifth entangled mode pair. (g) Measurement with all entangled comb lines turned on. Measured squeezing factors range from 2.1 to 2.8 dB, and the antisqueezing factors range from 9.3 to 13.3 dB. (h) Squeezing and antisqueezing levels across the spectrum from 3 to 21 MHz for all comb lines measured simultaneously. The detector's electrical noise is 18 dB below the vacuum noise. The resolution bandwidth is set to 300 kHz, and the video bandwidth to 300 Hz.

quantum advantage over the spectrum of interest, 3–21 MHz used to obtain Figs. 3–5.

In our experiment, the entangled signal comb is generated with a total power of 4 nW [Fig. 3(a)], consisting of ten signal comb lines alongside a central comb line with a power of 2 μW used to lock the phase between the entangled comb and the classical signal comb. To reduce beat-note phase noise, the signal comb power is reduced to sub-nW [Figs. 3(b) and 3(c)]. The entangled signal comb is measured using an LO comb with an average power of 1.8 mW per comb line.

3. Dual-comb spectra

The dual-comb spectra shown in Figs. 3(a)–3(c) and 4(b)–4(d) are derived by sampling the time-domain signal of the subtracted photocurrents from the balanced receiver. The signal is sampled at a rate of 100 MHz over a duration of 0.5 s. The recorded data are postprocessed to obtain the corresponding frequency-domain spectra. For Fig. 3(a), a resolution bandwidth of 10 kHz and 5000 interferograms are used in the postprocessing. In contrast, Figs. 3(b) and 3(c) employ a resolution bandwidth of 200 Hz with 100 interferograms, while Figs. 4(b)–4(d) use a resolution bandwidth of 100 Hz with 50 interferograms.

APPENDIX B: THEORY OF EDCS

We formulate the quantum theory model and present the formula of the photocurrent measurement readout, along with the derivations of the information-carrying mean, the quantum measurement noise, and finally the SNR.

1. Formulation of input and channel

Following the formalism in Ref. [26], we summarize the quantum theory for dual-comb spectroscopy with $2N+1$ comb lines for each comb, including a central comb line used solely for phase locking and N pairs of comb lines, symmetrically residing across the central line, for spectroscopy, as shown in Fig. 9. We assume that each comb line is effectively monochromatic; i.e., the frequency-comb linewidth is smaller than the minimum resolvable linewidth $1/T$, for acquisition T, such that each excited comb line can be regarded as a single frequency-bin mode. We require $f_{\mathrm{rep}}, \delta f_{\mathrm{ref}} > 1/T$ to avoid aliasing. Since the LO comb is much stronger than the signal comb, it is treated classically, fully characterized by its comb line amplitudes B_n at frequency nf_{rep} for $-N \le n \le N$. In contrast, the signal comb is characterized by line amplitudes $\{A_n\}$ and zero-mean quantum fluctuation modes $\{\hat{a}_{n,m}\}$. The power of the signal amounts to $P \equiv \hbar\omega_c \sum_{n=-N,n\neq 0}^{N} |A_n|^2/T$, where ω_c is the angular frequency of the optical carrier.

We now formally define the quantum fluctuation modes. The frequency modes of the field represented by the annihilation operators $\hat{a}_{n,m}$ satisfy the commutation relation $[\hat{a}_{n,m}, \hat{a}^{\dagger}_{n,m}] = 1$, while all other commutators are zero. Each

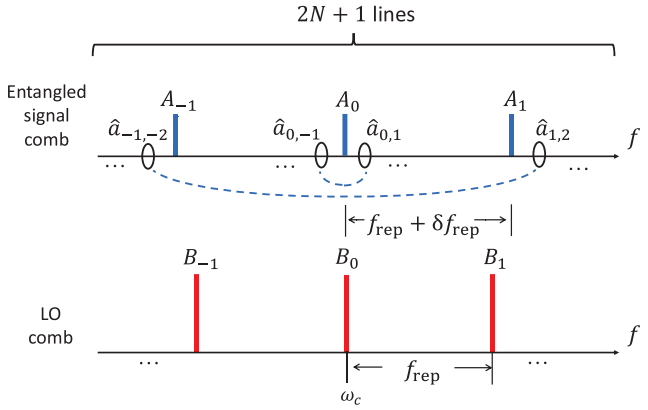

FIG. 9. Schematic of the frequency modes for the entangled signal comb and the local oscillator comb.

double subscript $n \in [-N, N]$ and $m \in [-N, N]$ indexes a mode at frequency $nf_{\mathrm{rep}} + m\delta f_{\mathrm{rep}}$. Here, n indexes the comb line that the mode is associated with, while m further identifies the mode relative to that line in its sideband. As $\delta f_{\mathrm{rep}} \gg 1/T$, the sideband modes around different comb lines will not overlap. These N^2 modes pertain to the EDCS data produced by the heterodyne measurement. In the classical DCS, the statistics of all modes are in the vacuum state, resulting in the classical shot-noise limit in heterodyne measurement. In contrast, the entanglement across different modes in EDCS enables surpassing the classical limit, as elaborated below.

We model the sample absorption process, whose transmissivity spectrum is to be measured, as a tensor product of bosonic loss channels. The input-output relation of such channel is $A_n \to \sqrt{\kappa_n} A_n e^{i\alpha_n}$ for means and

$$\hat{a}'_{n,m} = \sqrt{\kappa_n} e^{i\alpha_n} \hat{a}_{n,m} + \sqrt{1-\kappa_n}\,\hat{e}_{n,m} \tag{B1}$$

for noise modes, where κ_n and α_n are the power transmissivity and phase shift, respectively, of the absorption spectrum in the vicinity of frequency nf_{rep}.

2. Balanced heterodyne photocurrent

In the balanced heterodyne measurement, the LO comb beats with the returned signal comb on a balanced beam splitter. The beam splitter outputs are directed onto photodiodes, and the resulting photocurrents are subtracted to produce the rf photocurrent, denoted as $\hat{N}_{\mathrm{AC}}$, with the dc component discarded. Assuming strong LO, $B_n \gg A_m, \ \forall\ n, m$, the discrete Fourier spectrum of the balanced heterodyne photocurrent at rf frequency $m\delta f_{\mathrm{rep}}$ is

$$\hat{N}^{\mathrm{AC}}_m = \sum_{n=-N}^{N} B^*_n \hat{A}'_{n,m} + B_n \hat{A}'^{\dagger}_{n,-m}, \tag{B2}$$

where

$$\hat{A}'_{n,k} = \hat{a}'_{n,k} + \delta_{n,k}\sqrt{\kappa_n}A_n e^{i\alpha_n} \tag{B3}$$

is the returned signal spectrum at frequency $nf_{\mathrm{rep}} + k\delta f_{\mathrm{rep}}$. Here, the Kronecker delta $\delta_{n,k} = 1$ for $k = n$ and zero otherwise, and the channel output noises $\hat{a}'_{n,k}$ are defined by Eq. (B1). It contains two components—mean $\langle \hat{N}_m^{\mathrm{AC}} \rangle$ and zero-mean noise $\hat{\Sigma}_m^{\mathrm{AC}}$:

$$\hat{N}_m^{\mathrm{AC}} = \langle \hat{N}_m^{\mathrm{AC}} \rangle + \hat{\Sigma}_m^{\mathrm{AC}}. \tag{B4}$$

The output of the OPO forms pairs of two-mode squeezed states between $\hat{a}_{n,m}$ and $\hat{a}_{-n,-m}$. Let $\hat{a}_{n,m} \to \hat{a}_1$, $\hat{a}_{-n,-m} \to \hat{a}_2$, and one observes that the contribution to the noise $\hat{\Sigma}_m^{\mathrm{AC}}$ from the input is proportional to $(\hat{a}_1 + \hat{a}_2^\dagger)/\sqrt{2} = (\hat{q}_1 + \hat{q}_2)/\sqrt{2} + i(\hat{p}_1 - \hat{p}_2)/\sqrt{2} = \hat{q}_+ + i\hat{p}_-$, in the limit of $\kappa_n \to 1$. Thus, the noise on both quadratures can be suppressed by the two-mode squeezed state owing to the cross-mode entanglement, which does not violate Heisenberg uncertainty because $[\hat{q}_+, \hat{p}_-] = 0$. Later, we derive the complete formula in Eq. (B15).

3. Derivation of the mean of the balanced heterodyne photocurrent

The information about the absorption spectrum is encoded in the mean of the balanced heterodyne photocurrent. From Eq. (B2), we obtain the mean photocurrent

$$\begin{aligned}\langle \hat{N}_m^{\mathrm{AC}} \rangle &= \sum_{n=-N}^{N} \langle B_n^* \hat{A}'_{n,m} + B_n \hat{A}'^{\dagger}_{n,-m} \rangle \\ &= B_m^* \sqrt{\kappa_m} A_m e^{i\alpha_m} + B_{-m}\sqrt{\kappa_{-m}} A_{-m}^* e^{-i\alpha_{-m}}.\end{aligned} \tag{B5}$$

Equation (B5) suggests that the absorption on both the positive- and negative-index comb lines, $\sqrt{\kappa_m}e^{i\alpha_m}$, $\sqrt{\kappa_{-m}}e^{-i\alpha_{-m}}$, contributes to $\hat{N}_m^{\mathrm{AC}}$, causing aliasing. We next analyze aliasing-mitigation strategies.

4. Two-shot measurement without prior knowledge

To decode the absorption on the positive- and negative-index comb lines, i.e., $\sqrt{\kappa_m}e^{i\alpha_m}$ and $\sqrt{\kappa_{-m}}e^{-i\alpha_{-m}}$ concurrently, one adopts a two-shot measurement protocol. The first shot proceeds as described at the outset, producing photocurrent

$$\langle \hat{N}_m^{\mathrm{AC}(1)} \rangle = B_m^* \sqrt{\kappa_m} A_m e^{i\alpha_m} + B_{-m}\sqrt{\kappa_{-m}} A_{-m}^* e^{-i\alpha_{-m}}. \tag{B6}$$

In the second shot, a phase shift of π is applied to the positive-index classical comb lines, yielding $A_m \to -A_m$ for all $1 \le m \le N$ prior to combining it with the entangled comb. The heterodyne measurement produces photocurrent

$$\langle \hat{N}_m^{\mathrm{AC}(2)} \rangle = -B_m^* \sqrt{\kappa_m} A_m e^{i\alpha_m} + B_{-m}\sqrt{\kappa_{-m}} A_{-m}^* e^{-i\alpha_{-m}}. \tag{B7}$$

Subsequently, two linear combinations of $\sqrt{\kappa_m}e^{i\alpha_m}$, $\sqrt{\kappa_{-m}}e^{-i\alpha_{-m}}$ allow one to solve for both spectral components.

5. One-shot measurement with known phase

When the absorption phase spectrum $\{\alpha_m\}_{m=-N}^N$ is known or small, one lets $\{\alpha_m = 0\}_{m=-N}^N$ without loss of generality. Further assuming A_m's are real for $1 < m \le N$ and pure imaginary for $-N \le m < -1$, and B_m's are real, which can be attained by the wave shaper, the positive- and negative-index comb lines can be independently decoded in the real and imaginary components [$\cos(m\delta f_{\mathrm{rep}} t)$ and $\sin(m\delta f_{\mathrm{rep}} t)$ in the experiment] of the readout photocurrent:

$$\langle \hat{N}_m^{\mathrm{AC}} \rangle = B_m \sqrt{\kappa_m} A_m + iB_{-m}\sqrt{\kappa_{-m}} A_{-m}. \tag{B8}$$

6. Single-sided absorption

If the absorption is known to be on only positive- or negative-index comb lines, a single measurement suffices to infer the absorption spectrum. Without loss of generality, we assume the positive-index comb lines are lossless, i.e., $\kappa_{-m} = 1$ for $1 \le m \le N$, reducing the mean photocurrent in Eq. (B5) to

$$\langle \hat{N}_m^{\mathrm{AC}} \rangle = B_m^* \sqrt{\kappa_m} e^{i\alpha_m} A_m + B_{-m} A_{-m}^*. \tag{B9}$$

If $A_m = A_{-m} = A$ and $B_m = B_{-m} = B, \alpha_m = 0$, then

$$\langle \hat{N}_m^{\mathrm{AC}} \rangle = (1 + \sqrt{\kappa_m})AB. \tag{B10}$$

7. Derivation of the quantum measurement noise in the balanced heterodyne photocurrent

Because of asymmetric loss $\kappa_n \ne \kappa_{-n}$, antisqueezing noise contaminates the output. For simplicity, let $\alpha_n = 0$ for all $-N \le n \le N$ and $\theta_n = 0$ for $1 \le n \le N$, $\theta_n = \pi/2$ for $-N \le n \le -1$. We can divide the quantum noise $\hat{\Sigma}_m^{\mathrm{AC}}$ in photocurrent into two independent parts as $\hat{\Sigma}_m^{\mathrm{AC}} = \hat{\Sigma}_{m,Q}^{\mathrm{AC}} + \hat{\Sigma}_{m,P}^{\mathrm{AC}}$, where $\hat{\Sigma}_{m,Q}^{\mathrm{AC}}$ is the position quadrature contribution and $\hat{\Sigma}_{m,P}^{\mathrm{AC}}$ is the momentum quadrature contribution. At the strong LO limit, $\hat{\Sigma}_{m,Q}^{\mathrm{AC}}$ is

$$\begin{aligned}\sqrt{2}\hat{\Sigma}_{m,Q}^{\mathrm{AC}} \simeq\ & (B_0^* \hat{q}'_{0,m} + B_0 \hat{q}'_{0,-m}) \\ & + \sum_{n=1}^{N} [(B_n^* \hat{q}'_{n,m} + B_n \hat{q}'_{n,-m}) \\ & + (B_{-n}\hat{q}'_{-n,-m} + B_{-n}^* \hat{q}'_{-n,m})]\end{aligned} \tag{B11}$$

and, similarly,

$$\sqrt{2}\hat{\Sigma}^{\mathrm{AC}}_{m,P} \simeq i\Big\{(B_0^*\hat{p}'_{0,m} - B_0\hat{p}'_{0,-m}) + \sum_{n=1}^{N}[(B_n^*\hat{p}'_{n,m} - B_n\hat{p}'_{n,-m}) + (-B_{-n}\hat{p}'_{-n,-m} + B_{-n}^*\hat{p}'_{-n,m})]\Big\}, \tag{B12}$$

where $\hat{q}'_{n,m} \equiv \sqrt{2}\mathrm{Re}\hat{a}'_{n,m}$, $\hat{p}'_{n,m} \equiv \sqrt{2}\,\mathrm{Im}\,\hat{a}'_{n,m}$, and $\hat{a}'_{n,m} = \sqrt{\kappa_n}\hat{a}_{n,m} + \sqrt{1-\kappa_n}\hat{e}_{n,m}$ as defined in Eq. (B1). To describe the two-mode squeezing pairs $\hat{a}_{n,m}$ and $\hat{a}_{-n,-m}$, we define the common and differential modes, with the quadrature operators $\hat{q}^{\pm}_{n,m} \equiv \hat{q}_{n,m} \pm \hat{q}_{-n,-m}, \hat{p}^{\pm}_{n,m} \equiv \hat{p}_{n,m} \pm \hat{p}_{-n,-m}$. Then, two-mode squeezing can be described by the squeezed and antisqueezed quadratures

$$\mathrm{Var}\{\hat{q}^{+}_{n,m}\} = \mathrm{Var}\{\hat{p}^{-}_{n,m}\} = 1/G_n,$$
$$\mathrm{Var}\{\hat{q}^{-}_{n,m}\} = \mathrm{Var}\{\hat{p}^{+}_{n,m}\} = G'_n, \tag{B13}$$

where $G_n > 1$ specifies the amount of squeezing while $G'_n > 1$ quantifies the amount of antisqueezing. $G'_n \neq G_n > 1$ due to loss.

Owing to the symmetry between the Q and P contributions, we take one for SNR analyses as an example. After the transformations of $\hat{q}^{\pm}$ and $\hat{p}^{\pm}$, Eq. (B12) becomes

$$\begin{aligned}\sqrt{2}\hat{\Sigma}^{\mathrm{AC}}_{m,P}/i \simeq{}& B_0\sqrt{\kappa_0}\hat{p}^{-}_{0,m} + \sum_{n=1}^{N}\left[\sqrt{\kappa_n}\left(B_n^*\frac{\hat{p}^{+}_{n,m}+\hat{p}^{-}_{n,m}}{2} - B_n\frac{\hat{p}^{+}_{n,-m}+\hat{p}^{-}_{n,-m}}{2}\right)\right.\\ &\left.+\sqrt{\kappa_{-n}}\left(-B_{-n}\frac{\hat{p}^{+}_{n,m}-\hat{p}^{-}_{n,m}}{2} + B_{-n}^*\frac{\hat{p}^{+}_{n,-m}-\hat{p}^{-}_{n,-m}}{2}\right)\right] + \text{environment}\\ ={}& B_0\sqrt{\kappa_0}\hat{p}^{-}_{0,m} + \sum_{n=1}^{N}\frac{1}{2}\left[(\sqrt{\kappa_n}B_n^* - \sqrt{\kappa_{-n}}B_{-n})\hat{p}^{+}_{n,m} + (-\sqrt{\kappa_n}B_n + \sqrt{\kappa_{-n}}B_{-n}^*)\hat{p}^{+}_{n,-m}\right.\\ &\left.+(\sqrt{\kappa_n}B_n^* + \sqrt{\kappa_{-n}}B_{-n})\hat{p}^{-}_{n,m} + (-\sqrt{\kappa_n}B_n - \sqrt{\kappa_{-n}}B_{-n}^*)\hat{p}^{-}_{n,-m}\right] + \text{environment},\end{aligned} \tag{B14}$$

where the environment contributes a variance of $\sum_{n=-N}^{N}(1-\kappa_n)B_n^2$. Finally, the variance of the momentum-quadrature contribution is

$$\mathrm{Var}\hat{\Sigma}^{\mathrm{AC}}_{m,P} = \frac{1}{2}\kappa_0|B_0|^2\frac{1}{G_0} + \sum_{n=1}^{N}\frac{1}{4}[|\sqrt{\kappa_n}B_n^* - \sqrt{\kappa_{-n}}B_{-n}|^2G'_n + |\sqrt{\kappa_n}B_n^* + \sqrt{\kappa_{-n}}B_{-n}|^2/G_n] + \frac{1}{2}\sum_{n=-N}^{N}(1-\kappa_n)|B_n|^2, \tag{B15}$$

and similar for the variance of position-quadrature contribution. Plugging vacuum-state input with no squeezing $G_n = G'_n = 1$ in Eq. (B15), we obtain the shot (vacuum) noise limit

$$\sigma^2_{\mathrm{SHOT}} = \mathrm{Var}\hat{\Sigma}^{\mathrm{AC}}_{m,Q}|_{G_n=G'_n=1} = \mathrm{Var}\hat{\Sigma}^{\mathrm{AC}}_{m,P}|_{G_n=G'_n=1} = \frac{1}{2}\sum_{n=-N}^{N}\kappa_n|B_n|^2 + (1-\kappa_n)|B_n|^2 = \frac{1}{2}\sum_{n=-N}^{N}|B_n|^2, \tag{B16}$$

which is determined by the total LO comb power $P_{\mathrm{LO}} = \hbar\omega_c\sum_{n=-N}^{N}|B_n|^2/T$.

8. SNR analyses

To calculate the SNR at the mth line, we define the signal power as $|B_m^*\sqrt{\kappa_m}A_m|^2$ in the rf photocurrent that can be modulated by $\sqrt{\kappa_m}e^{i\alpha_m}$. For a one-shot measurement with a known phase, the mean photocurrent is given by Eq. (B8). In this case, the signal power is defined as the power of the measured mean of the real quadrature of the photocurrent at the mth line. For the single-sided absorption measurement with prior knowledge, where the photocurrent mean is given by Eq. (B9), this can be obtained using a single-sided signal comb, i.e., $A_m = 0$ for $m \leq 0$. Combining Eqs. (B5) and (B15) by assuming $\alpha_m, \alpha_{-m} \to 0$, the power SNR for estimating the spectrum $\sqrt{\kappa_m}$ at the mth line is

$$\mathrm{SNR}^2_m = \frac{|B_m^*\sqrt{\kappa_m}A_m|^2}{\frac{1}{2}\kappa_0|B_0|^2\frac{1}{G_0} + \sum_{n=1}^{N}\frac{1}{4}[|\sqrt{\kappa_n}B_n^* - \sqrt{\kappa_{-n}}B_{-n}|^2G'_n + |\sqrt{\kappa_n}B_n^* + \sqrt{\kappa_{-n}}B_{-n}|^2/G_n] + \mathrm{vac}}, \tag{B17}$$

where vac $= \frac{1}{2}\sum_{n=-N}^{N}(1-\kappa_n)|B_n|^2$ arises from vacuum noise mixed in due to sample absorption.

A single comb line from the entangled signal comb is too weak to be measured precisely. Hence, its power is inferred from the rf photocurrent obtained in a calibration measurement with B_m known, $\kappa_{-m} = 1$. With A_m inferred from experimental data, we obtain the absolute SNR curve shown in Fig. 6 in the main text.

9. Classical limits of DCS

In DCS, the SNR is determined by both the entanglement structure and the measurement scheme. Below, we present two examples.

a. Entangled DCS and heterodyne receiver

In this paper, EDCS employs a total power of $P = \hbar\omega_c A^2 M/T$ on the sample in an asymmetric configuration, where only the signal comb impinges on the sample, and exploits a heterodyne receiver for measurement. It yields an amplitude SNR as derived by Eq. (B17). Assuming uniform comb spectrum $A_n = A, B_n = B$ and weak absorption $\kappa_n \to 1$, the CL for the SNR for asymmetric DCS is, thus,

$$(\mathrm{SNR}_{\mathrm{CL}}^{\mathrm{asym}})^2 = \frac{A^2}{M/2} = \frac{2PT}{M^2\hbar\omega_c}. \tag{B18}$$

b. Squeezed DCS and division receiver

Reference [27]'s squeezed DCS first combines the signal and LO combs on a 50:50 beam splitter to produce a total power of $P = \hbar\omega_c(A^2 + B^2)M/2T$ impinging on the sample, followed by a division receiver. In such a *symmetric* DCS configuration [14], both combs pass through the sample and typically carry comparable amount of optical power. As such, we no longer assume LO comb is much more intense than the signal comb; namely, A_n and B_m can be on the same order. Assuming uniform comb spectrum $A_n = A, B_n = B$ and weak absorption $\kappa_n \to 1$, it yields the SNR for symmetric DCS as derived in Ref. [52]:

$$(\mathrm{SNR}^{\mathrm{sym}})^2 = \frac{1}{M}\frac{A^2B^2}{2B^2\sigma_B^2 + 2A^2\sigma_A^2}, \tag{B19}$$

where the factor of 2 arises from the beating with both positive- and negative-index comb lines, $\sigma_A^2 \equiv \mathrm{var}\mathrm{Re}\hat{a}_{n,m}$ is the phase-known field fluctuation, similar for σ_B. Note that, in Ref. [52], the fluctuations were defined as $\sigma_A^2 \equiv \mathrm{var}\mathrm{Re}\hat{a}_{n,m} + \mathrm{var}\,\mathrm{Im}\,\hat{a}_{n,m}$, where the phase-unknown case was considered; thus, the noise contained both quadratures, and the power SNR was halved. Setting $\sigma_A^2 = \sigma_B^2 = 1/4$ to the shot-noise limit, the attainable classical SNR with Ref. [27]'s experimental setup is

$$(\mathrm{SNR}_{\mathrm{C}}^{\mathrm{sym}})^2 = \frac{1}{M}\frac{2A^2B^2}{B^2 + A^2}, \tag{B20}$$

which is maximized by simply setting $A^2 = B^2 = PT/M\hbar\omega_c$, i.e., having two combs with equal power on the sample, yielding the classical limit for the SNR as

$$(\mathrm{SNR}_{\mathrm{CL}}^{\mathrm{sym}})^2 = \frac{PT}{M^2\hbar\omega_c}. \tag{B21}$$

However, Ref. [27]'s experiment employs two combs with vastly different power levels at $A^2 = 15$ mW and $B^2 = 10$ μW to interrogate the sample, leading to an SNR that is at least 22 dB below the CL attained by interrogating the sample with equal amount of power for both combs while keeping the total power fixed, even with the 3-dB enhancement enabled by squeezing one of the combs accounted for. In the experiment, the measurement noise predominately stems from the more intense comb, whose squeezing reduces the noise floor, whereas the other much weaker comb does not contribute to the measurement noise. To substantially increase the SNR, one may opt to balance the power of the two combs. However, in doing so, additional noise may create challenges that hinder the quantum advantage of the experimental system. As such, to surpass the CL of DCS, a meticulously designed entanglement structure between the comb lines is required, as demonstrated in the present EDCS experiment.

[1] A. Einstein, B. Podolsky, and N. Rosen, *Can quantum-mechanical description of physical reality be considered complete?*, Phys. Rev. **47**, 777 (1935).

[2] E. Schrödinger, *Discussion of probability relations between separated systems*, in *Mathematical Proceedings of the Cambridge Philosophical Society* (Cambridge University Press, Cambridge, England, 1935), Vol. 31, pp. 555–563.

[3] J. S. Bell, *On the Einstein Podolsky Rosen paradox*, Phys. Phys. Fiz. **1**, 195 (1964).

[4] Z. Zhang, C. You, O. S. Magaña-Loaiza, R. Fickler, R. d. J. León-Montiel, J. P. Torres, T. S. Humble, S. Liu, Y. Xia, and Q. Zhuang, *Entanglement-based quantum information technology: A tutorial*, Adv. Opt. Photonics **16**, 60 (2024).

[5] R. Jozsa and N. Linden, *On the role of entanglement in quantum-computational speed-up*, Proc. R. Soc. A **459**, 2011 (2003).

[6] A. K. Ekert, *Quantum cryptography based on Bell's theorem*, Phys. Rev. Lett. **67**, 661 (1991).

[7] T. C. Ralph, *Continuous variable quantum cryptography*, Phys. Rev. A **61**, 010303(R) (1999).

[8] E. S. Polzik, J. Carri, and H. J. Kimble, *Spectroscopy with squeezed light*, Phys. Rev. Lett. **68**, 3020 (1992).

[9] Y. Xia, W. Li, W. Clark, D. Hart, Q. Zhuang, and Z. Zhang, *Demonstration of a reconfigurable entangled radio-frequency photonic sensor network*, Phys. Rev. Lett. **124**, 150502 (2020).

[10] X. Guo, C. R. Breum, J. Borregaard, S. Izumi, M. V. Larsen, T. Gehring, M. Christandl, J. S. Neergaard-Nielsen, and U. L. Andersen, *Distributed quantum sensing in a continuous-variable entangled network*, Nat. Phys. **16**, 281 (2020).

[11] S. Hao, H. Shi, C. N. Gagatsos, M. Mishra, B. Bash, I. Djordjevic, S. Guha, Q. Zhuang, and Z. Zhang, *Demonstration of entanglement-enhanced covert sensing*, Phys. Rev. Lett. **129**, 010501 (2022).
[12] T. B. Pittman, Y. H. Shih, D. V. Strekalov, and A. V. Sergienko, *Optical imaging by means of two-photon quantum entanglement*, Phys. Rev. A **52**, R3429 (1995).
[13] N. Picqué and T. W. Hänsch, *Frequency comb spectroscopy*, Nat. Photonics **13**, 146 (2019).
[14] I. Coddington, N. Newbury, and W. Swann, *Dual-comb spectroscopy*, Optica **3**, 414 (2016).
[15] E. D. Caldwell, L. C. Sinclair, N. R. Newbury, and J.-D. Deschenes, *The time-programmable frequency comb and its use in quantum-limited ranging*, Nature (London) **610**, 667 (2022).
[16] M. Takamoto, F.-L. Hong, R. Higashi, and H. Katori, *An optical lattice clock*, Nature (London) **435**, 321 (2005).
[17] Z. Jiang, C.-B. Huang, D. E. Leaird, and A. M. Weiner, *Optical arbitrary waveform processing of more than 100 spectral comb lines*, Nat. Photonics **1**, 463 (2007).
[18] B. Xu, Z. Chen, T. W. Hänsch, and N. Picqué, *Near-ultraviolet photon-counting dual-comb spectroscopy*, Nature (London) **627**, 289 (2024).
[19] M. Walsh, P. Chang, F. Emaury, G. Rieker, N. Newbury, F. Giorgetta, S. Diddams, and J. Genest, *Mode-resolved, shot noise limited, dual-comb spectroscopy with independent free running lasers*, in *Fourier Transform Spectroscopy* (Optica Publishing Group, Munich, Germany, 2023), pp. JTh1A–1.
[20] S. Camenzind, B. Sierro, B. Willenberg, A. Nussbaum-Lapping, A. Rampur, U. Keller, A. Heidt, and C. R. Phillips, *Shot-noise limited dual-comb supercontinuum*, Opt. Open **112418** (2024).
[21] M. Tse, H. Yu, N. Kijbunchoo, A. Fernandez-Galiana, P. Dupej, L. Barsotti, C. Blair, D. Brown, S. Dwyer, A. Effler *et al.*, *Quantum-enhanced Advanced LIGO detectors in the era of gravitational-wave astronomy*, Phys. Rev. Lett. **123**, 231107 (2019).
[22] Y. Xia, W. Li, Q. Zhuang, and Z. Zhang, *Quantum-enhanced data classification with a variational entangled sensor network*, Phys. Rev. X **11**, 021047 (2021).
[23] Y. Xia, A. R. Agrawal, C. M. Pluchar, A. J. Brady, Z. Liu, Q. Zhuang, D. J. Wilson, and Z. Zhang, *Entanglement-enhanced optomechanical sensing*, Nat. Photonics **17**, 470 (2023).
[24] Z. Zhang, S. Mouradian, F. N. C. Wong, and J. H. Shapiro, *Entanglement-enhanced sensing in a lossy and noisy environment*, Phys. Rev. Lett. **114**, 110506 (2015).
[25] A. Belsley, *Quantum-enhanced absorption spectroscopy with bright squeezed frequency combs*, Phys. Rev. Lett. **130**, 133602 (2023).
[26] H. Shi, Z. Chen, S. E. Fraser, M. Yu, Z. Zhang, and Q. Zhuang, *Entanglement-enhanced dual-comb spectroscopy*, npj Quantum Inf. **9**, 91 (2023).
[27] D. I. Herman, M. Walsh, M. K. Kreider, N. Lordi, E. J. Tsao, A. J. Lind, M. Heyrich, J. Combes, J. Genest, and S. A. Diddams, *Squeezed dual-comb spectroscopy*, Science **387**, 653 (2025).
[28] V. Giovannetti, S. Lloyd, and L. Maccone, *Advances in quantum metrology*, Nat. Photonics **5**, 222 (2011).
[29] S. Steinlechner, J. Bauchrowitz, M. Meinders, H. Müller-Ebhardt, K. Danzmann, and R. Schnabel, *Quantum-dense metrology*, Nat. Photonics **7**, 626 (2013).
[30] M. Chen, N. C. Menicucci, and O. Pfister, *Experimental realization of multipartite entanglement of 60 modes of a quantum optical frequency comb*, Phys. Rev. Lett. **112**, 120505 (2014).
[31] D. Walls and G. Milburn, *Quantum Optics 2nd Edition*, St Lucia, Brisbane QLD (Springer, 2011), 4072.
[32] D. I. Herman, M. K. Kreider, N. Lordi, M. Walsh, E. J. Tsao, A. J. Lind, M. Heyrich, J. Combes, S. A. Diddams, and J. Genest, *Phase-dependent squeezing in dual-comb interferometry*, arXiv:2506.18698.
[33] I. E. Gordon, L. S. Rothman, e. R. Hargreaves, R. Hashemi, E. V. Karlovets, F. Skinner, E. K. Conway, C. Hill, R. V. Kochanov, Y. Tan *et al.*, *The HITRAN2020 molecular spectroscopic database*, J. Quant. Spectrosc. Radiat. Transfer **277**, 107949 (2022).
[34] A. Parriaux, K. Hammani, and G. Millot, *Electro-optic frequency combs* Adv. Opt. Photonics **12**, 223 (2020).
[35] X. Jia, C. Zhai, X. Zhu, C. You, Y. Cao, X. Zhang, Y. Zheng, Z. Fu, J. Mao, T. Dai *et al.*, *Continuous-variable multipartite entanglement in an integrated microcomb*, Nature (London) **639**, 329 (2025).
[36] Y. Shen, P.-Y. Hsieh, S. K. Sridhar, S. Feldman, Y.-C. Chang, T. A. Smith, and A. Dutt, *Strong nanophotonic quantum squeezing exceeding 3.5 dB in a foundry-compatible Kerr microresonator*, Optica **12**, 302 (2025).
[37] Z. Wang, K. Li, Y. Wang, X. Zhou, Y. Cheng, B. Jing, F. Sun, J. Li, Z. Li, B. Wu *et al.*, *Large-scale cluster quantum microcombs*, Light Sci. Appl. **14**, 164 (2025).
[38] Y. Zhang, M. Menotti, K. Tan, V. Vaidya, D. Mahler, L. Helt, L. Zatti, M. Liscidini, B. Morrison, and Z. Vernon, *Squeezed light from a nanophotonic molecule*, Nat. Commun. **12**, 2233 (2021).
[39] S. Liu, A. Hariri, B.-H. Wu, Y. Zhang, and Z. Zhang, *Generation of squeezed light in silicon nitride photonic integrated chips*, in *CLEO: Fundamental Science* (Optica Publishing Group, 2024), pp. FF2H–6.
[40] M. Jahanbozorgi, Z. Yang, S. Sun, H. Chen, R. Liu, B. Wang, and X. Yi, *Generation of squeezed quantum microcombs with silicon nitride integrated photonic circuits*, Optica **10**, 1100 (2023).
[41] H. Vahlbruch, M. Mehmet, K. Danzmann, and R. Schnabel, *Detection of 15 dB squeezed states of light and their application for the absolute calibration of photoelectric quantum efficiency*, Phys. Rev. Lett. **117**, 110801 (2016).
[42] E. Lucas, S.-P. Yu, T. C. Briles, D. R. Carlson, and S. B. Papp, *Tailoring microcombs with inverse-designed, meta-dispersion microresonators*, Nat. Photonics **17**, 943 (2023).
[43] S.-P. Yu, D. C. Cole, H. Jung, G. T. Moille, K. Srinivasan, and S. B. Papp, *Spontaneous pulse formation in edgeless photonic crystal resonators*, Nat. Photonics **15**, 461 (2021).
[44] R. Moreira, S. Gundavarapu, and D. J. Blumenthal, *Programmable eye-opener lattice filter for multi-channel dispersion compensation using an integrated compact*

low-loss silicon nitride platform, Opt. Express **24**, 16732 (2016).

[45] A. Dutt, C. Joshi, X. Ji, J. Cardenas, Y. Okawachi, K. Luke, A. L. Gaeta, and M. Lipson, *On-chip dual-comb source for spectroscopy*, Sci. Adv. **4**, e1701858 (2018).

[46] G. Millot, S. Pitois, M. Yan, T. Hovhannisyan, A. Bendahmane, T. W. Hänsch, and N. Picqué, *Frequency-agile dual-comb spectroscopy*, Nat. Photonics **10**, 27 (2016).

[47] E. Deriushkina, I. Rebolledo-Salgado, M. Mazur, V. Torres-Company, P. Andrekson, J. Schröder, and M. Karlsson, *Dual-comb swept-wavelength interferometry: Theory and experiment*, J. Lightwave Technol. **40**, 6508 (2022).

[48] V. Durán, P. A. Andrekson, and V. Torres-Company, *Electro-optic dual-comb interferometry over 40 nm bandwidth*, Opt. Lett. **41**, 4190 (2016).

[49] A. S. Kowligy, D. R. Carlson, D. D. Hickstein, H. Timmers, A. J. Lind, P. G. Schunemann, S. B. Papp, and S. A. Diddams, *Mid-infrared frequency combs at 10 GHz*, Opt. Lett. **45**, 3677 (2020).

[50] M. Yan, Z. Wan, Y. Chen, X. Zhang, and H. Zeng, *Quantum correlation-enhanced dual-comb spectroscopy*, Light Sci. Appl. **14**, 257 (2025).

[51] T. Ralph, *Can signal-to-noise be improved by heterodyne detection using an amplitude squeezed local oscillator?*, Phys. Rev. Lett. **85**, 677 (2000).

[52] H. Shi *et al.* (to be published).